Assessment of the impact of modeling axial compression on PET image reconstruction

Martin A. Belzunce[a)] and Andrew J. Reader
Division of Imaging Sciences & Biomedical Engineering, King's College London, St Thomas' Hospital, London SE1 7EH, UK

(Received 7 March 2017; revised 28 June 2017; accepted for publication 29 June 2017;
published 11 August 2017)

Purpose: To comprehensively evaluate both the acceleration and image-quality impacts of axial compression and its degree of modeling in fully 3D PET image reconstruction.
Method: Despite being used since the very dawn of 3D PET reconstruction, there are still no extensive studies on the impact of axial compression and its degree of modeling during reconstruction on the end-point reconstructed image quality. In this work, an evaluation of the impact of axial compression on the image quality is performed by extensively simulating data with span values from 1 to 121. In addition, two methods for modeling the axial compression in the reconstruction were evaluated. The first method models the axial compression in the system matrix, while the second method uses an unmatched projector/backprojector, where the axial compression is modeled only in the forward projector. The different system matrices were analyzed by computing their singular values and the point response functions for small subregions of the FOV. The two methods were evaluated with simulated and real data for the Biograph mMR scanner.
Results: For the simulated data, the axial compression with span values lower than 7 did not show a decrease in the contrast of the reconstructed images. For span 11, the standard sinogram size of the mMR scanner, losses of contrast in the range of 5–10 percentage points were observed when measured for a hot lesion. For higher span values, the spatial resolution was degraded considerably. However, impressively, for all span values of 21 and lower, modeling the axial compression in the system matrix compensated for the spatial resolution degradation and obtained similar contrast values as the span 1 reconstructions. Such approaches have the same processing times as span 1 reconstructions, but they permit significant reduction in storage requirements for the fully 3D sinograms. For higher span values, the system has a large condition number and it is therefore difficult to recover accurately the higher frequencies. Modeling the axial compression also achieved a lower coefficient of variation but with an increase of intervoxel correlations. The unmatched projector/backprojector achieved similar contrast values to the matched version at considerably lower reconstruction times, but at the cost of noisier images. For a line source scan, the reconstructions with modeling of the axial compression achieved similar resolution to the span 1 reconstructions.
Conclusions: Axial compression applied to PET sinograms was found to have a negligible impact for span values lower than 7. For span values up to 21, the spatial resolution degradation due to the axial compression can be almost completely compensated for by modeling this effect in the system matrix at the expense of considerably larger processing times and higher intervoxel correlations, while retaining the storage benefit of compressed data. For even higher span values, the resolution loss cannot be completely compensated possibly due to an effective null space in the system. The use of an unmatched projector/backprojector proved to be a practical solution to compensate for the spatial resolution degradation at a reasonable computational cost but can lead to noisier images. [https://doi.org/10.1002/mp.12454]

Key words: axial compression, PET, resolution modeling, span, system matrix, unmatched projectors

1. INTRODUCTION

Traditionally, in 3D positron emission tomography (PET), axial compression is often used to reduce the computational requirements of the image reconstruction algorithms.[1] Nowadays, due to the progress in computational power, most PET scanners use list-mode or span-1 reconstructions.[2–5] However, in 4D reconstruction, the computational cost and storage requirements for a time-series consisting of up to 30 frames of fully 3D sinogram data are still too demanding,[6,7] and hence a data compression method is still needed in order to reconstruct images in a practical time. For this reason, axial compression is still used in some scanners or reconstruction frameworks to reduce the data size of each scan and the computation times during reconstruction. For time-of-flight (TOF) scanners, the number of sinogram bins is even larger and axial compression can be applied directly during the list-mode

acquisition.[3] Axial compression is achieved by averaging a set of sinograms with adjacent values of the oblique polar angle[1] (see Fig. 1). This sampling scheme achieves good results in the center of the field of view (FOV). However, there is a loss in the radial, tangential, and axial resolution at off-center positions, which is greater for scanners with larger FOVs.

Despite being used since the beginning of 3D PET reconstruction, there are no extensive studies of the effect of the axial compression, and its compensation through reconstruction, on image quality and resolution, except for the rebinning methods that convert 3D data into multislice 2D sinograms.[8–10] In TOF scanners, the use of TOF axial rebinning algorithms can also cause resolution loss but to a reduced extent.[11,12] In addition, when the data have already been axially compressed during acquisition, the degradation of resolution can be compensated for if this process is modeled in the system matrix.[13] To model the axial compression correctly in the system matrix involves using span-1 projectors, which are computationally very demanding. The computational burden can be reduced if an unmatched projector/backprojector strategy is used, where the projector models the axial compression and the backprojector does not. It has been shown that using an unmatched projector/backprojector in the maximum likelihood expectation maximization (MLEM) algorithm is valid under suitable conditions[14,15] and it has been proposed before to reduce the reconstruction times by using a full model in the forward projector and a simpler one in the backprojector.[16–19]

When axial compression is applied, the point spread function (PSF) is extremely shift-variant for high span values. Therefore, special attention needs to be taken to the effect of modeling the axial compression in the system matrix, that is a special case of resolution modeling. The latter usually shows an enhancement of the contrast and an improvement in the resolution of the reconstructed images.[20] An apparent noise reduction is also observed, but at the cost of modifying the noise structure and introducing higher intervoxel correlations.[20,21] Furthermore, resolution modeling suffers from Gibbs artifacts and can make the reconstruction problem under-determined.[22] A possible reason for this effect is that the imaging system has an effective null space and therefore the higher frequencies cannot be properly recovered. This effect was studied by Tong et al.[23] where the condition number and rank for different resolution kernels were analyzed only in image space. Therefore, studying the condition number and rank of system matrices that model the axial compression is a useful tool to have a better insight into this process.

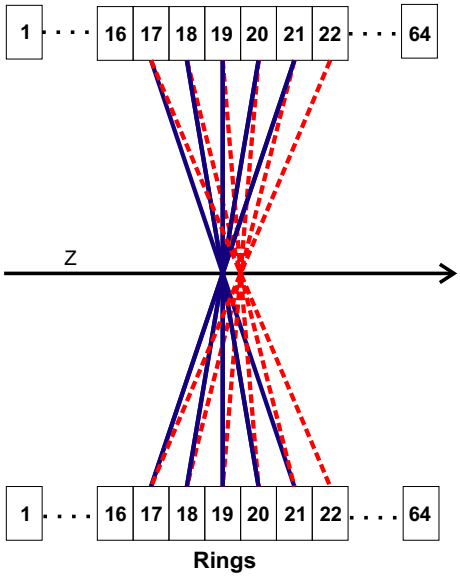

FIG. 1. Example of a span 11 axial compression in segment 0 for a scanner with 64 rings. In solid lines, five sinogram planes are compressed into the direct plane sinogram for ring 19. In dashed lines, six sinogram planes are compressed into an intermediate position sinogram located between rings 19 and 20. [Color figure can be viewed at wileyonlinelibrary.com]

In this work, we conduct an exhaustive assessment of the impact of different span choices on spatial resolution, image quality, and computational cost of the axial compression and its modeling in the system matrix that is used in image reconstruction algorithms. This analysis is useful for deciding the sinogram size when doing reconstructions with large datasets, such as motion-corrected 4D PET reconstructions. In addition, when sinograms are acquired directly with axial compression, we importantly demonstrate that the image quality degradation can be compensated for by including a model of that process in the reconstruction, provided the longer processing time is accommodated. Furthermore, we propose an unmatched projector/backprojector reconstruction to reduce the computational cost of modeling the axial compression in the reconstruction. The different system matrices used in this work were analyzed using the singular value decomposition (SVD) for small subregions of the FOV. The singular value spectrum, along with the point response function (PRF) modeled in the system matrix, were utilized to look into the effects of the axial compression and its modeling in the system matrix. Simulated data of the Biograph mMR scanner were reconstructed to assess the image quality and convergence of each method. The contrast and coefficient of variation (COV) were plotted as function of the iteration number for every expectation maximization (EM) reconstruction. The image resolution achieved with each method was also assessed using real data of a line source scan.

2. MATERIALS AND METHODS

An assessment of the impact of axial compression on image quality was performed by simulating datasets for the Biograph mMR PET-MR scanner (Siemens Healthcare, Erlangen, Germany).[24] Additionally, we studied the effect of modeling the axial compression in the system matrix employing two different methods. The singular value spectrum of each system matrix, as well as the PRF, were used to have a better insight into the effects of axial compression and its modeling. For each span value simulated, we reconstructed the images, with and without modeling the axial

compression, using the maximum likelihood expectation maximization (MLEM) algorithm.[25] The reconstruction methods were also evaluated with real data of a line source scan.

2.A. The Biograph mMR scanner

The Biograph mMR scanner has 64 rings and admits lines of response (LORs) with a maximum ring difference of 60. It has a transaxial FOV of 59.4 cm and an axial FOV of 25.8 cm. Each acquisition can be configured in list or sinogram mode. The system uses a sinogram-based reconstruction with an axial compression of span 11 and a component-based normalization.[26] Additionally, the scanner stores span 1 sinograms in interfile format for each acquisition with both prompts and delayed events in separate sets of sinograms. This feature brings the possibility of implementing image reconstruction algorithms without axial compression (span 1) or with any other span.

The default span 11 sinograms have a total of 837 sinogram planes arranged in 11 segments (Fig. 1 shows an example of the axial compression applied in segment 0). Each sinogram plane has 344 [radial coordinate] $\times$ 252 [azimuthal angle] bins, as no transverse mashing is applied. For the span 1 sinograms, the number of sinogram planes is 4084 arranged in 121 segments occupying a total of 708 MBytes compared to the 125 MBytes of the span 11 sinograms.

2.B. Image reconstruction

A C++ reconstruction library with the MLEM and the ordinary Poisson ordered subsets expectation maximization (OP-OSEM)[27] algorithms was developed for the Biograph mMR. The library uses a projector/backprojector based on the Siddon algorithm that was implemented for any span and for CPU and GPU platforms.[28]

The GPU version was developed in CUDA using a parallelization scheme based on a one thread per ray strategy. The sinograms were stored in global memory due to the large amount of memory required. The image is stored in texture memory for the forward projector in order to improve the memory access bandwidth. This is not possible in the backprojector as the texture memory is read-only. Moreover, the backprojector uses atomic instructions to avoid race-condition problems.[28] As a result, the projector is more than 5$\times$ faster than the backprojector (Fig. 2). The reconstructions were run using the GPU implementation on a NVIDIA Quadro K5200 and the reconstruction times were recorded for every case.

2.C. Modeling the axial compression in the system matrix

In the MLEM reconstruction, the standard forward model includes the attenuation, normalization, scatter, and random effects.[29] Therefore, each iteration is described by:

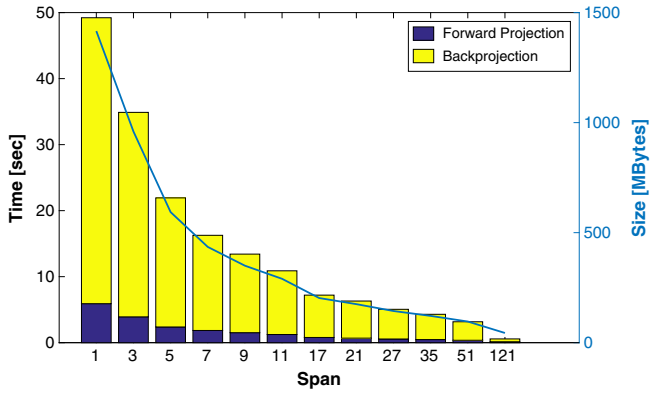

FIG. 2. MLEM iteration time for each sinogram size. The total iteration time is split into the forward projection (blue) and the backprojection (yellow) times. The storage size in MBytes for each span value is shown on a blue line using the right y-axis. [Color figure can be viewed at wileyonlinelibrary.com]

$$f^{k+1} = \frac{f^k}{X_a^t L_a N_a 1} X_a^t L_a N_a \frac{b_a}{N_a L_a X_a f^k + s + r} \tag{1}$$

where f^k is a vector with the reconstructed image in iteration k, b_a is the vector containing the span-a emission sinograms, X_a is the x-ray transform that projects image f^k into span-a sinograms, L_a and N_a are diagonal matrices with the attenuation and normalization factors respectively, 1 is a unit-valued column vector of the same size of the sinogram, and s and r are vectors with the mean scatter and randoms estimates respectively.

To include the effect of the axial compression in the system matrix, we introduced a compression matrix C_a that compresses a span-1 sinogram into span-a. Therefore the EM iteration is replaced by the following equation:

$$f^{k+1} = \frac{f^k}{X_1^t L_1 N_1 C_a^t 1} X_1^t L_1 N_1 C_a^t \frac{b_a}{C_a N_1 L_1 X_1 f^k + s + r} \tag{2}$$

where X_1 is the x-ray transform for span-1 sinograms and b_a is the vector containing the span-a emission sinograms. We call this method MLEM-MAC (MLEM with modeled axial compression), and it uses a span 1 projector, backprojector, and normalization.

For the case where the normalization factors are only available in the original size of the emission sinograms, the system model used by the algorithm must be approximated according to:

$$f^{k+1} = \frac{f^k}{X_1^t C_a^t L_a N_a 1} X_1^t C_a^t L_a N_a \frac{b_a}{N_a L_a C_a X_1 f^k + s + r} \tag{3}$$

where N_a and L_a are the normalization and attenuation factors for a span a sinogram. For the normalization factors used in this work, the differences in the reconstructed images between Eqs. (2) and (3) were negligible. Therefore, from here on all the reconstructions with the MLEM-MAC method were performed using Eq. (2).

2.D. Modeling axial compression in an unmatched projector/backprojector reconstruction

Reconstruction algorithms (2) and (3) are both computationally very intensive. The use of a complete forward model and a simpler backprojector, in an unmatched projector reconstruction, has been proposed before to reduce the computational cost of each iteration.[16–19] In a similar way, we propose inclusion of the axial compression model only in the forward projection:

$$f^{k+1} = \frac{f^k}{X_a^t L_a N_a 1} X_a^t L_a N_a \frac{b_a}{N_a L_a C_a X_1 f^k + s + r} \tag{4}$$

where X_a is the x-ray transform for span-a sinograms. We call this method MLEM-MAC-U. This scheme uses a span-1 forward projector and a span-a backprojector, reducing the computational cost compared to the complete modeling of the axial compression by avoiding a span 1 backprojection in each iteration.

2.E. Singular value decomposition of the system matrices

We carried out a spectral comparison between the different system matrices (A) used in this work by computing their singular values using the SVD. This task is not feasible for a full system matrix because of their extremely large size. For that reason, we computed the SVD for smaller system matrices that model the acquisition process only in small subregions of the FOV. Subregions with a size of $8 \times 8 \times 8$ pixels centered in different regions of the field of view were used. When applying axial compression, a voxel in the FOV is affected mainly by the values of the neighboring voxels. For this reason, using system matrices for only small patches can still provide a useful insight into the condition number of the full system matrix. Only the LORs that intersect voxels of the small subregion were considered in each of the computed system matrices (i.e., only 1×10^6 sinogram bins for span 1).

Figure 3 plots, on a logarithmic scale, the singular values for the span 1, span 11, and span 121 system matrices, with and without axial compression modeling, for a subregion of $8 \times 8 \times 8$ pixels located in the center of the FOV. In Fig. 4 the singular values are plotted for a subregion centered at (0,130,0) mm in the FOV. In both figures, the condition number of each matrix is shown in the legends.

The system matrices with axial compression modeling (span 11-MAC and span 121-MAC, respectively) represent the response of a system that applies axial compression, where multiple oblique sinograms are assigned to a single direct or oblique sinogram. For these cases, we can see that the system has a larger condition number (computed as the ratio between the maximum and minimum singular values) for higher span values. This agrees with what is seen in resolution modeling, where for wider PSFs a higher condition number is obtained.[23] However, for the subregion of Fig. 3,

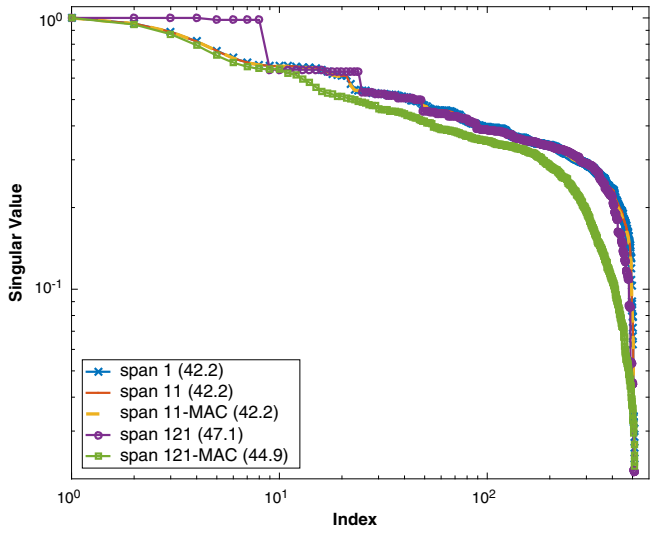

FIG. 3. Singular value spectrum of the span 1, span 11, span 121, span 11-MAC, and span 121-MAC system matrices for a subregion of $8 \times 8 \times 8$ voxels located in the centre of the FOV. In the legend, the condition number of each matrix is shown in brackets. [Color figure can be viewed at wileyonlinelibrary.com]

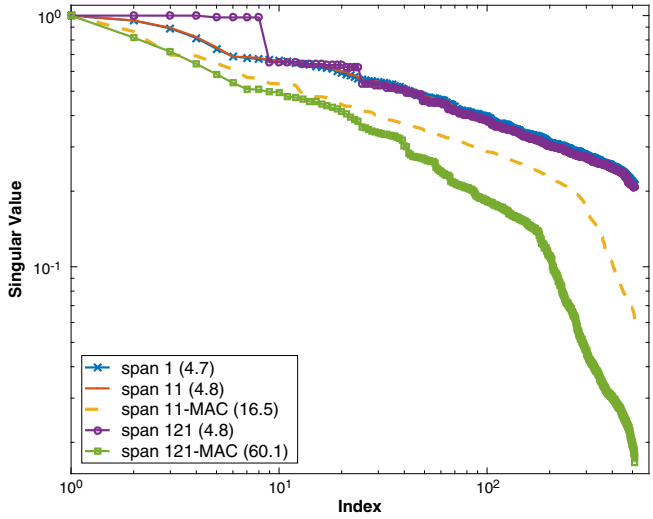

FIG. 4. Singular value spectrum of the span 1, span 11, span 121, span 11-MAC, and span 121-MAC system matrices for a subregion of $8 \times 8 \times 8$ voxels located at (0,130,0) mm. In the legend, the condition number of each matrix is shown in brackets. [Color figure can be viewed at wileyonlinelibrary.com]

the condition numbers for the different system matrices are very similar because axial compression has a negligible impact in the center of the FOV.

System matrices which do not include axial compression modeling have similar singular value spectra for any span (e.g., span 1, 11, and 121 in Fig. 4), but they do not have the same reconstruction performance for real data as they cannot recover the resolution degradation arising from the axial compression. Such matrices represent unrealistic systems that would correspond to acquiring LORs only along the exact directions of the oblique sinogram planes available for that

span. It is of interest to include these cases, as quite often such matrices are used in idealized simulation studies.

In addition, we compared between the correct modeling of axial compression (MAC) and the unmatched scheme (MAC-U) using the SVD of A^tA. Here we use the SVD of A^tA as for MAC-U, the transpose matrix (without resolution modeling) is only an approximation of the transpose of A, and therefore both matrices need to be evaluated together. For the MAC-U system matrix, we used $A_a^t A_{a-MAC}$, with:

$$A_{a-MAC} = C_a X_1 \tag{5}$$

In Fig. 5, the singular values of A^tA for span 121, span 121-MAC, and span 121-MAC-U are plotted. The condition number for the unmatched scheme (span 121-MAC-U) is extremely large, showing that this scheme is very ill-posed.

The SVD analysis shows that modeling the axial compression makes the system matrix more ill-conditioned and this is exacerbated for higher span values. For a certain noise level, the smaller singular values can be considered as an effective null space. On the other hand, the SVD spectrum for the span 1 and span 11 system matrices without modeling the axial compression are equivalent, and only slightly different for the extreme case of span 121. This means that if we simulate sinograms by projecting span a data and then we reconstruct it, we would achieve similar results to span 1 simulated and reconstructed data. This is an expected outcome as 3D reconstruction is an overdetermined problem.

Finally, the point response functions for each voxel modeled in the subregion system matrices were used to understand the correlation and the resolution degradation when axial compression is applied. The PRFs were obtained by computing the matrix A^tA, which contains the PRF for a given voxel in each of its columns. It is important to note that these PRFs do not correspond to reconstructed point spread functions (PSFs). Using the PRFs available in the small system matrices, we can examine how the axial compression averages pixels in different directions for different regions of the field of view. In the z axis, it can be easily understood how the axial compression works (e.g., consider again Fig. 1), but in the transverse direction it is not as intuitive. Figure 6 shows the PRF for the central pixel of subregions at the center (0,0,0) mm, at (0,130,0) mm, at (−130,0,0) mm, and at (−130,130,−64) mm for the span 1, span 11-MAC, and span 121-MAC system matrices. Each column of images represents the PRF for a system matrix located in one of the subregions, while the rows are the eight slices of each PRF. In Fig. 6 we can see that the pixels are correlated in the tangential direction. For example, in the second subregion (with $x = 0$ mm) of Fig. 6, the correlation occurs between columns, while in the third subregion (with $y = 0$ mm) occurs in rows.

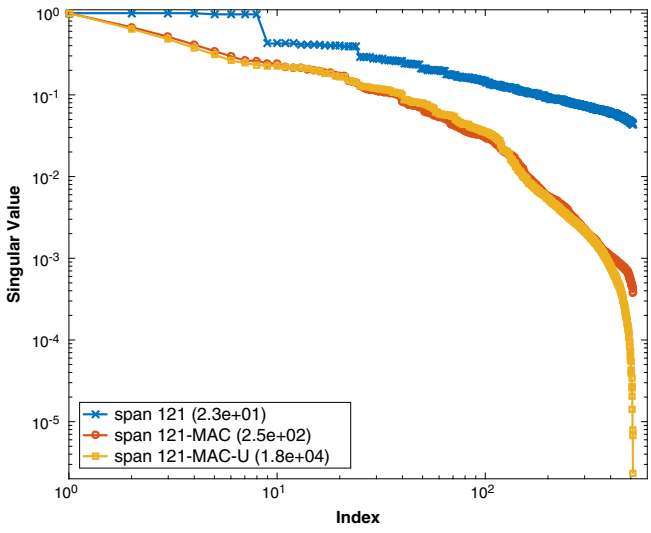

FIG. 5. Singular value spectrum of A^tA for the span 121, span 121-MAC, and span 121-MAC-U system matrices for a subregion of 8 × 8 × 8 voxels located at (0,130,0) mm. In the legend, the condition number of each matrix is shown in brackets. [Color figure can be viewed at wileyonlinelibrary.com]

2.F. Simulated data and image quality evaluation

We simulated 3D sinograms by projecting an NCAT[30] and a Defrise phantom[31] into span-1 sinograms. The detection efficiency of each line of response was simulated by multiplying each projected phantom by span 1 normalization factors, which were obtained by expanding a CBN file of the Biograph mMR scanner.[26] Next, we introduced noise to the sinograms by simulating a Poisson process; we scaled the sinograms to get mean values of 5 counts ($\lambda = 5$) and then generated Poisson distributed counts for each bin. Finally, we applied an axial compression to the span 1 noisy sinogram, using a range of 10 span values that varied from 3 to 121. The Defrise phantom contained 10 evenly-spaced disks of 10 mm height and 300 mm diameter, inside a cylinder of 210 mm height and 375 mm diameter (Fig. 7). The activity ratio between the disks and the background was 2:1.

For the NCAT phantom, we performed an additional simulation that takes into account the point spread function of the system. In this simulation, the phantom was convolved with a 4.5 mm FWHM Gaussian kernel prior to forward projection.

The simulated sinograms were reconstructed using the ordinary Poission MLEM algorithm and the two proposed methods to model the axial compression: MLEM-MAC and MLEM-MAC-U. The image quality parameters were computed for each of the 100 iterations with the objective of accommodating the different convergence rates of each method for a fair comparison. The simulations that included the system PSF were reconstructed without PSF modeling (MLEM and MLEM-MAC) and with PSF modeling in image space[32] (MLEM-PSF and MLEM-PSF-MAC).

For the Defrise phantom, we computed the contrast recovery (CR) for each disk using a ROI for each of them and one for the background. The contrast recovery was defined as:

$$CR_d = \frac{\frac{\mu_d}{\mu_b} - 1}{R_{d-b} - 1} \cdot 100\% \tag{6}$$

where CR_d is the contrast recovery of disk d, μ_d is the mean value of the disk d ROI, μ_b is the mean value of the background

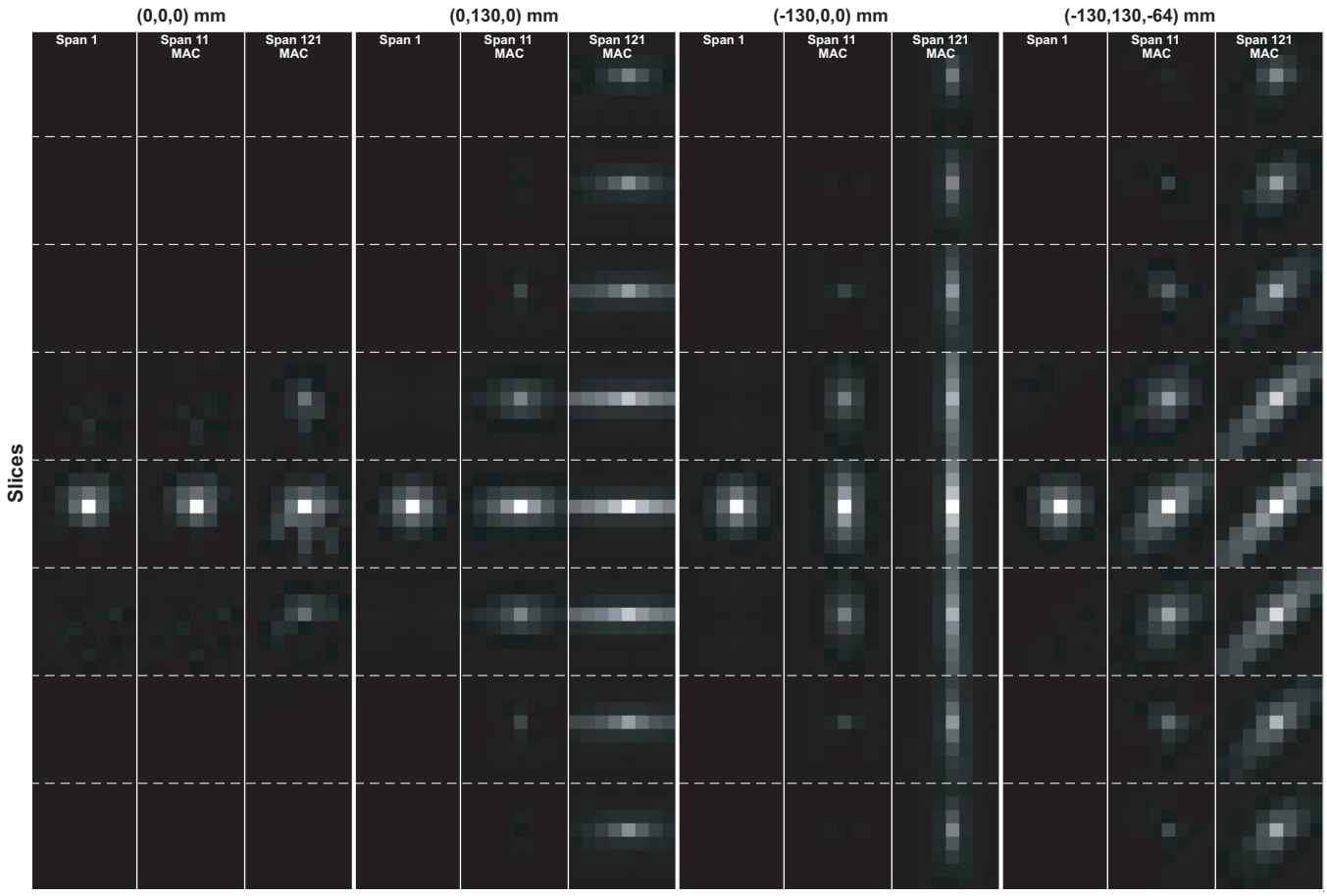

FIG. 6. Point response functions for the system matrices for span 1, span 11-MAC, and span 121-MAC for four different subregions centred at (0,0,0), (0,130,0), (−130,0,0), and (−130,0,0) in mm. Each PRF is shown in individual columns and the rows are transverse slices of each PRF.

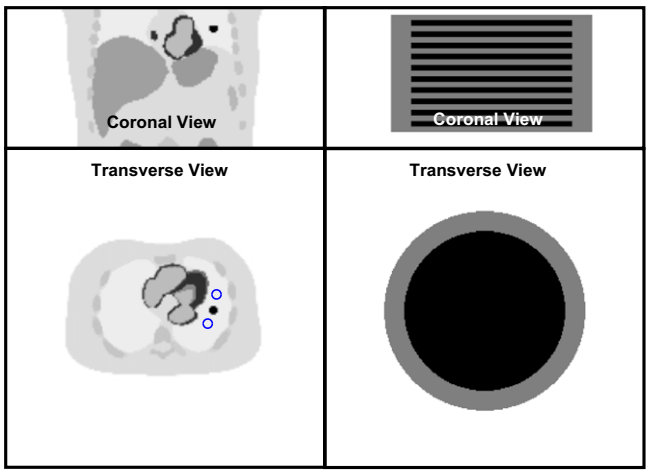

FIG. 7. On the left, coronal and transverse view of the NCAT phantom. In the transverse slice, the hot lesion used to evaluate the contrast is in black and the ROIs used for measuring the background are marked in blue. On the right, coronal and transverse view of the Defrise phantom. [Color figure can be viewed at wileyonlinelibrary.com]

ROI, and R_{d-b} is the true activity ratio between the disk and the background cylinder (equal to 2 in our simulations).

For the NCAT phantom, we computed the COV and the contrast recovery in a lesion in the lungs by using a ROI centered in the lesion and two ROIs in the background next to the lesion (Fig. 7). Each parameter was computed for every iteration of the three reconstruction methods. For this phantom, the analysis was repeated for a noise-free simulation and an additional noisy realization with $\lambda = 1$.

2.G. Line source scan

A line source was used to evaluate the impact on the spatial resolution of the axial compression and its modeling in the image reconstruction. The line source was located in a oblique direction in the FOV, where the line sweeps from −160 to + 180 mm in x, + 100 to + 105 mm in y and the whole axial length in z (Fig. 8). The images were reconstructed using the ordinary Poission MLEM algorithm and the two proposed methods to model the axial compression. The full width at half maximum (FWHM) in each direction was computed for each iteration.

The FWHM in the x and y axes were computed for each transverse slice and the FWHM in the y and z axes for each sagittal plane. The FWHM was computed using the coordinates of the maximum value for each plane, then analyzing each 1D profile centered in the maximum pixel for each axis and obtaining an interpolated coordinate value for the half of the maximum pixel value.

3. RESULTS

A comparison of the standard MLEM reconstruction for different span values is shown in Figs. 9 and 10, where the COV and CR are plotted as function of the iteration number for the Defrise and NCAT phantoms, respectively. It can be seen that performance is similar among the group of spans 1 to 5 (span 5 shows slightly better contrast than span 1), but that there is a notable degradation when span 11 is considered. For span 11, the contrast was approximately 10% less than for span 1, which is notable, as the standard mMR axial compression is span 11. The span 7 reconstruction achieved a similar contrast than span 11 for the hot lesion of the NCAT phantom but a higher contrast in the disks of the Defrise phantom.

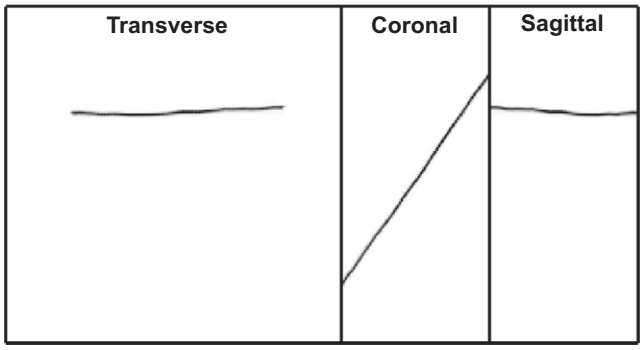

FIG. 8. Transverse, coronal, and sagittal maximum intensity projections of the line source scan.

Figure 11 looks at the convergence rate of the two reconstruction methods that model the axial compression during reconstruction, for span values of 1, 7, 11, 21, 51, and 121, by showing the CR and COV as a function of the iteration number for the NCAT phantom reconstructions. In these plots, the results for the standard MLEM reconstruction were also included. The span 1 [Fig. 11(a)] reconstructions were used as a reference to assess the proposed methods. These plots show that the method that fully model the axial compression (MLEM-MAC) has a slower convergence rate, as would be expected due to the overall less sparse system matrix, but it achieves the same contrast value as the span 1 reconstruction with a lower COV for span values lower to 21. The unmatched projector/backprojector method (MLEM-MAC-U), with the axial compression modeled only in the forward projector, improves the contrast considerably with a faster convergence rate than MLEM-MAC, but at a cost of increasing the noise. Similar results for the Defrise phantom are shown in Fig. 12.

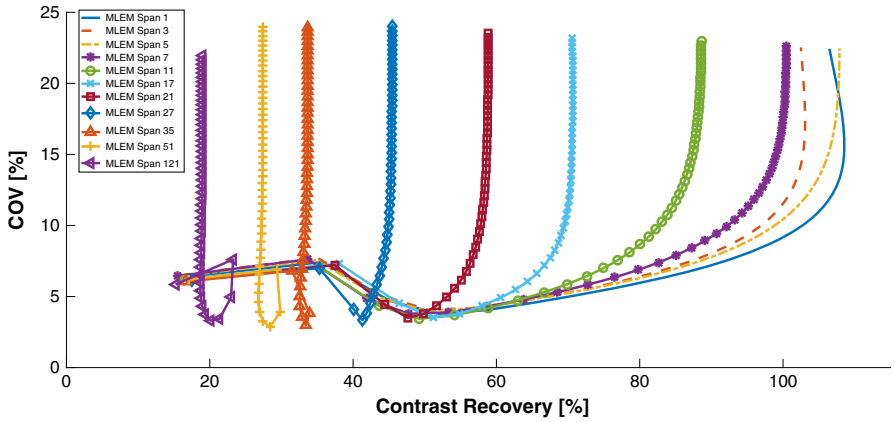

FIG. 9. COV and contrast recovery in disk number 5 as function of the iteration number for the standard MLEM reconstructions of the simulated sinograms for the Defrise phantom for all the span values used. [Color figure can be viewed at wileyonlinelibrary.com]

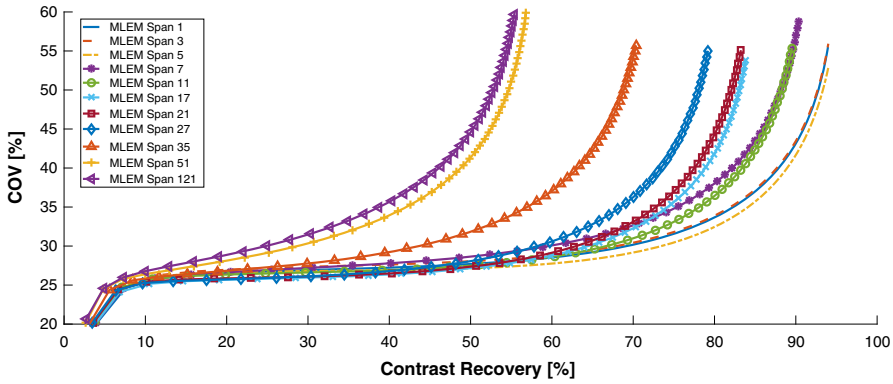

FIG. 10. COV and contrast recovery of the hot lesion as function of the iteration number for the standard MLEM reconstructions of the simulated sinograms for the NCAT phantom for all the span values evaluated. [Color figure can be viewed at wileyonlinelibrary.com]

Transverse and coronal images for the NCAT phantom for span 11 and span 51 are shown in Figs. 13 and 14, respectively. In both figures, the images for MLEM, MLEM-MAC, and MLEM-MAC-U were included. To avoid using a fixed iteration number for algorithms with different convergence rates, we selected images for matched COV, using the COV value of the MLEM-MAC at iteration 100 as the reference. Using the same methodology, the transverse and coronal slices for the Defrise phantom are shown in Fig. 15 for span values of 11 and 51, for the MLEM and MLEM-MAC reconstruction methods. It can be observed that the MLEM-MAC reconstructions have not completely converged at iteration number 100. For the span 51 images, the effect of resolution degradation is easily observed for the standard MLEM reconstruction. The improvement of the resolution with the method that models the axial compression is demonstrated in these images.

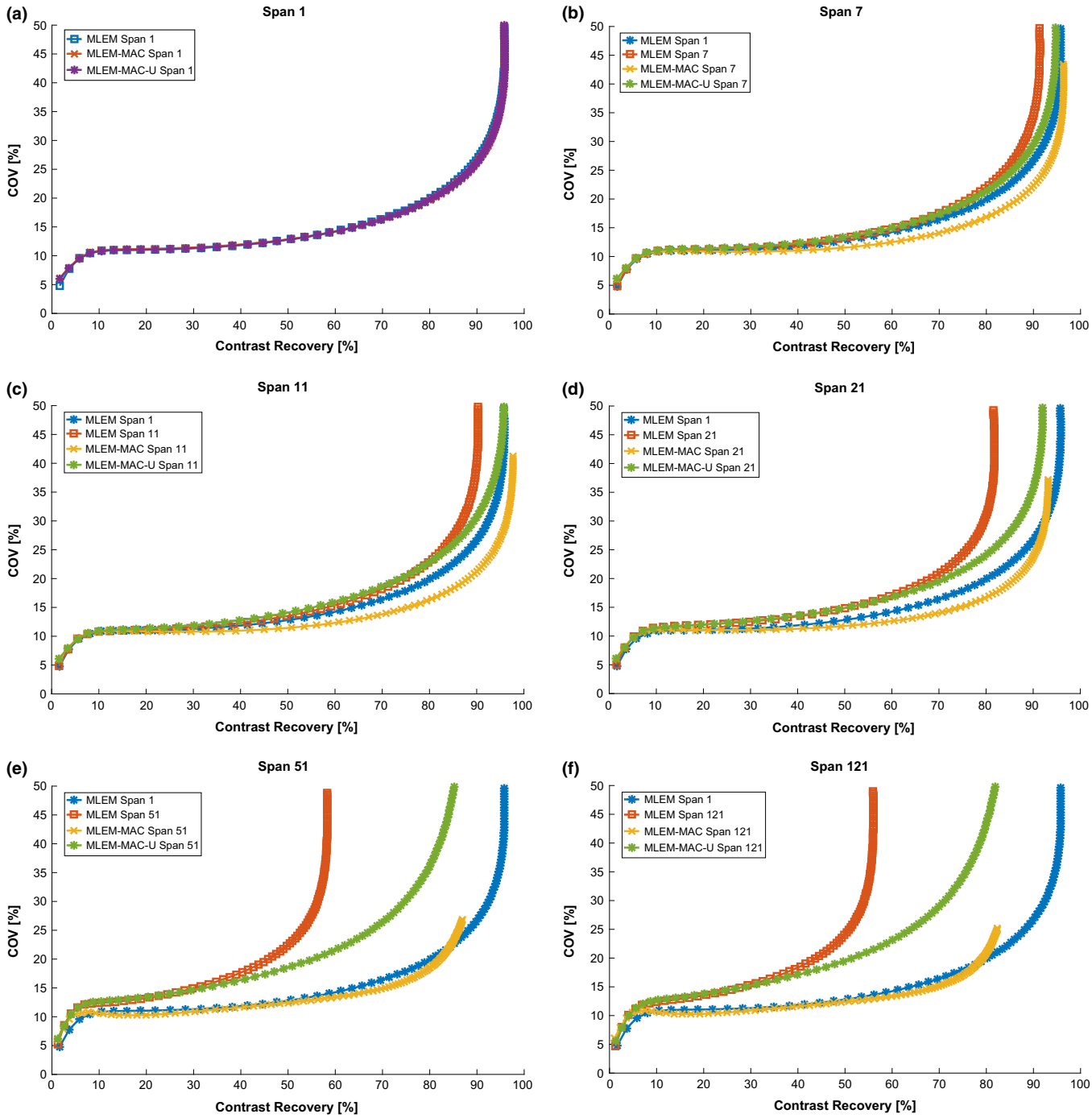

FIG. 11. COV and CR in the hot lesion of the reconstructed images of the NCAT phantom as function of the iteration number. The results for the simulations of span 1 sinogram data which are then compressed into span 7, 11, 21, 51, and 121 were included. [Color figure can be viewed at wileyonlinelibrary.com]

In Fig. 16, the reconstructed images for the simulations that included the system PSF are shown for the noise-free and noisy simulations. The reconstructions with PSF modeling only, with axial compression modeling only and then with both effects simultaneously modeled are shown. It can be seen that when only the PSF is modeled, there is a loss of resolution in the tangential direction which is recovered when axial compression is also modeled (third column).

For the line source scan, a comparison of the standard MLEM reconstruction for different span values is shown in Fig. 17, where the FWHM in the x and y axes are plotted as function of the iteration number for the transverse slice 30. We can observe that, for this line source, there is a considerable loss of the spatial resolution in the x axis but not in the y axis. These results are due to orientation of the line source, that is approximately parallel to the xz

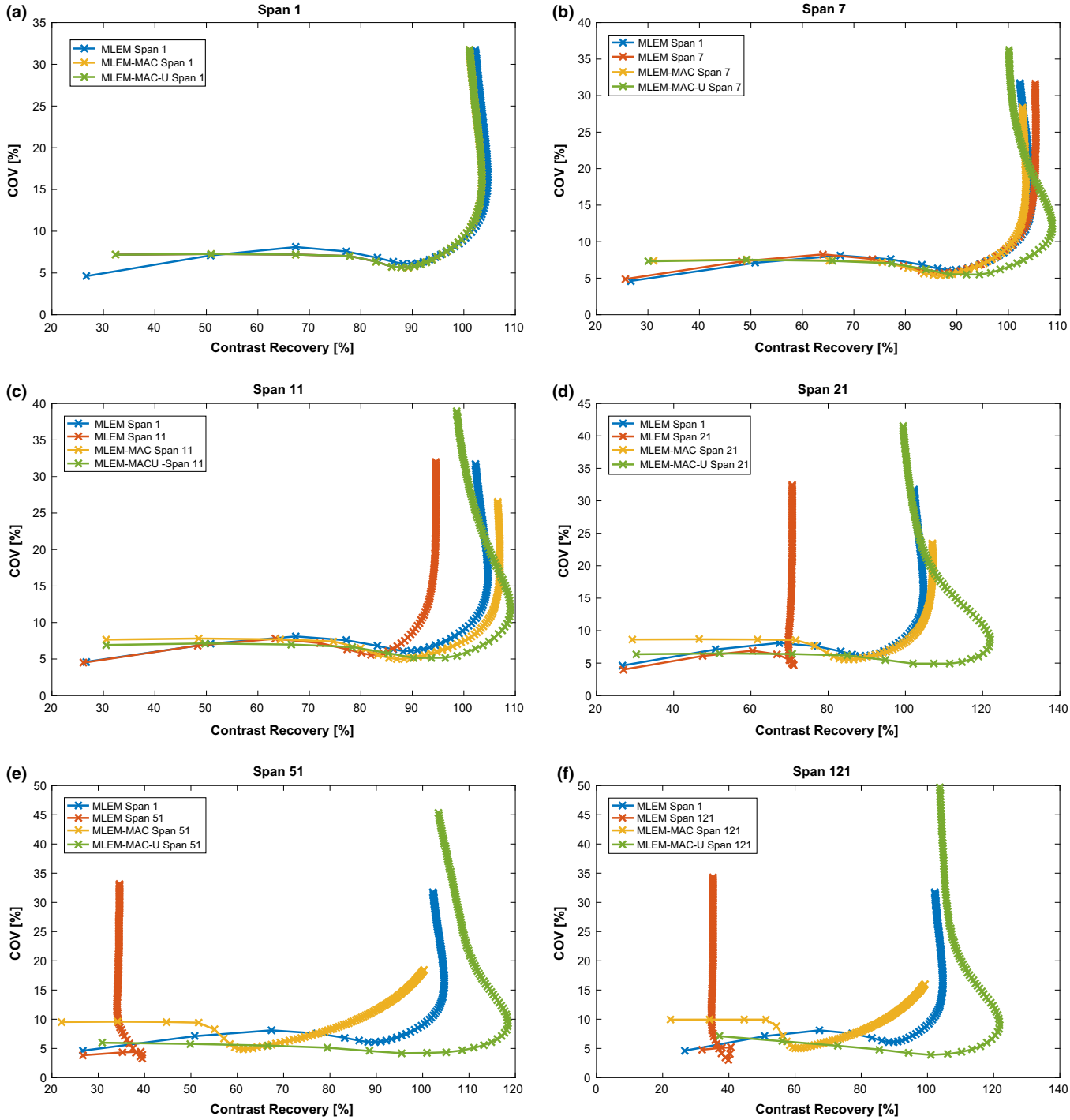

FIG. 12. COV and CR for disk number 1 of the reconstructed images of the Defrise phantom as function of the iteration number. The results for the simulations of sinograms with span values of 1, 7, 11, 21, 51, and 121 were included. [Color figure can be viewed at wileyonlinelibrary.com]

plane. A similar effect was observed in the sagittal plane, where the spatial resolution was degraded only in the z direction.

The FWHM values obtained when applying the two different methods to model the axial compression in the reconstruction are presented in Fig. 18. These results confirm the compensation of the spatial resolution degradation observed in the simulated datasets. The spatial resolution degradation due to the axial compression in the sinograms was successfully compensated for by the MLEM-MAC method, achieving comparable FWHM values to the span 1 reconstruction. We found that the unmatched projector/backprojector had some problems to recover the spatial resolution in some slices, as can be seen in the central slice for the span 121 reconstruction (Fig. 19), where the line source is split into two lines.

With respect to the processing times, Fig. 20 illustrates the iteration time and the maximum contrast recovery in the hot lesion for the reconstructed images of the NCAT phantom as a function of the span value. In the standard MLEM algorithm, from span 1 to span 7, there is a negligible impact on the contrast recovery but the processing time is reduced approximately four times. From span 7 to 11, the contrast recovery starts to decrease without an important reduction of the iteration time. From span 11 to 51, the contrast decreases considerably. The MLEM-MAC method takes almost a constant time for all the reconstructions, albeit equivalent to a span 1 reconstruction. The unmatched projector/backprojector reconstruction (MLEM-MAC-U) achieves a good contrast recovery with much lower reconstruction times,

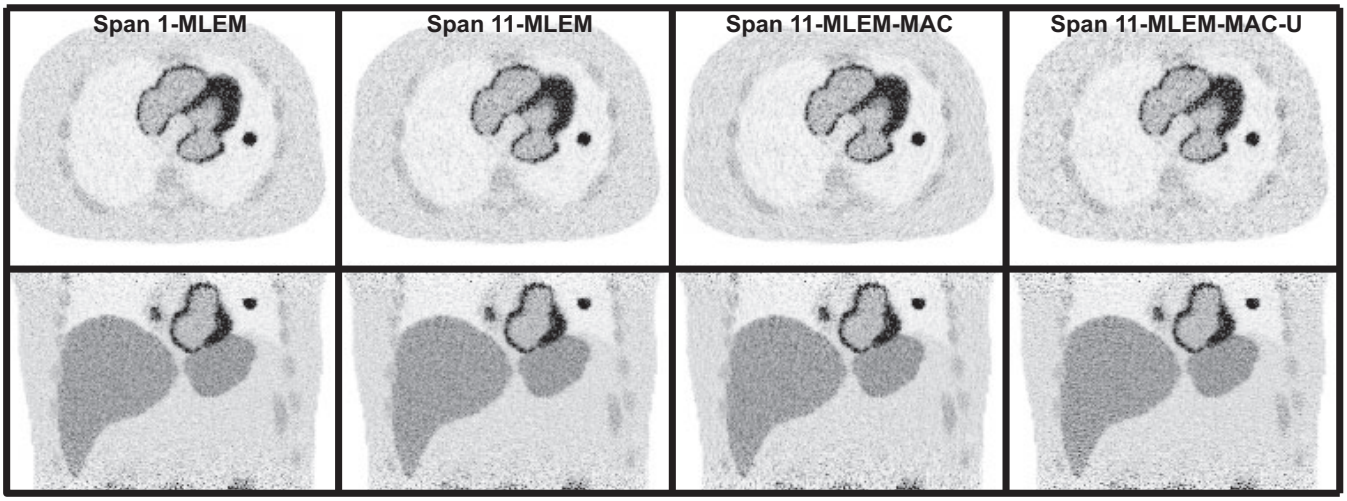

FIG. 13. Transverse (top row) and coronal (bottom row) slices of the reconstructed images from the NCAT phantom simulations with span 11 using three different reconstructions method: MLEM (middle-left), MLEM-MAC (middle-right), and MLEM-MAC-U (right). On the left column, the span 1 image is also presented as the best achievable result. The iteration number was selected to give matched COV (iterations 74, 75, 100, and 75 from left to right).

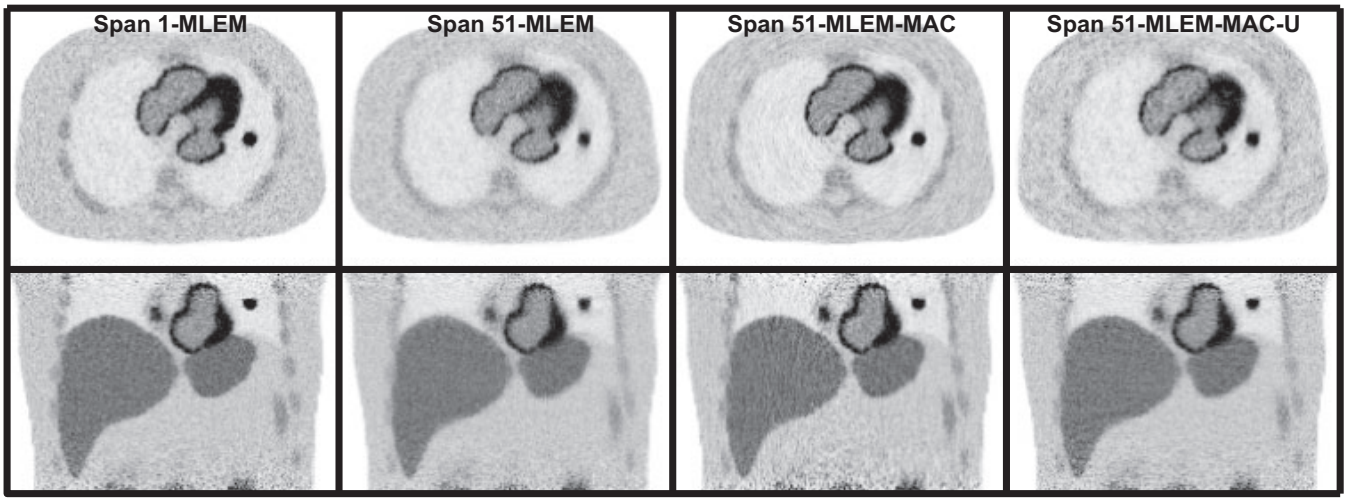

FIG. 14. Transverse (top row) and coronal (bottom row) slices of the reconstructed images from the NCAT phantom simulations with span 51 using three different reconstructions method: MLEM (middle-left), MLEM-MAC (middle-right), and MLEM-MAC-U (right). On the left column, the span 1 image is also presented as the best achievable result. The iteration number was selected to get matched COV (iterations 53, 36, 100, and 40 from left to right).

although at a cost of a higher noise as it has been shown previously.

4. DISCUSSION

The correct modeling of the axial compression (MLEM-MAC) using sinograms of up to span 21 achieved similar performance to span 1 reconstructions when using the contrast in the hot lesion as a metric and this is reflective of lesion detectability. Furthermore, the COV was lower in the background around the lesion for MLEM-MAC compared to span 1. However, the images show that the noise for MLEM-MAC seems to be correlated in a circular pattern (see Fig. 14). This pattern is related to the way that axial compression works in the transverse plane. In Fig. 6, the PRF for the method MAC shows that the axial compression blurs pixels only in the direction of x for a source on the y axis and vice versa; and for positions displaced both in x and y the blurring is along a diagonal direction. This results in spatial noise correlations, such as the circular texture seen in Fig. 14, can also give rise to a lower spatial COV, as observed in the MLEM-MAC reconstructions. As already known, resolution modeling (of

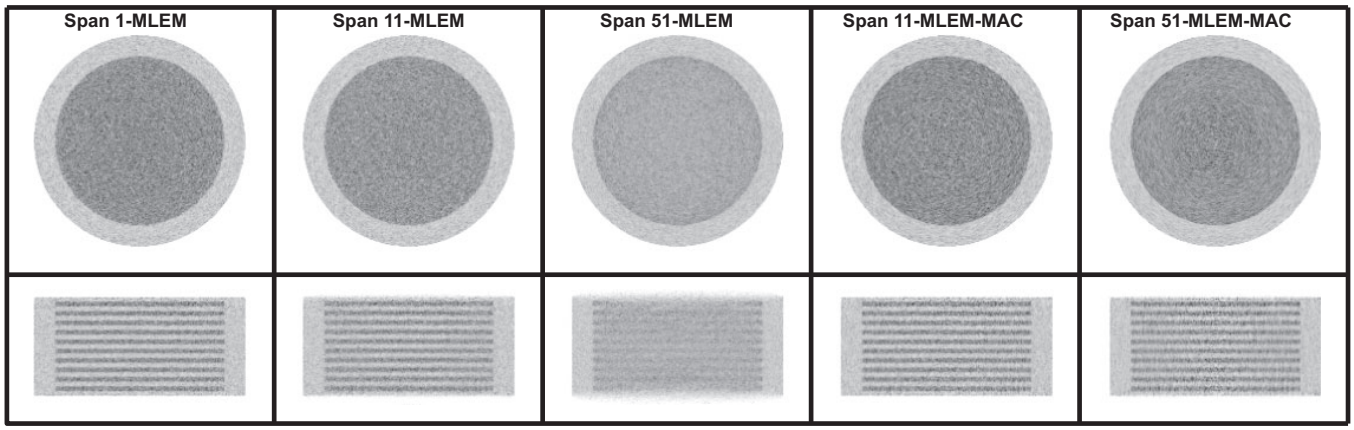

FIG. 15. Transverse (top row) and coronal (bottom row) slices of the reconstructed images from the Defrise phantom simulations with span 11 and span 51 using the MLEM and MLEM-MAC methods. In the left column, the span 1 image is also presented as the best achievable result. The iteration number was selected for matched COV (iterations 54, 53, 37, 76, and 99 from left to right).

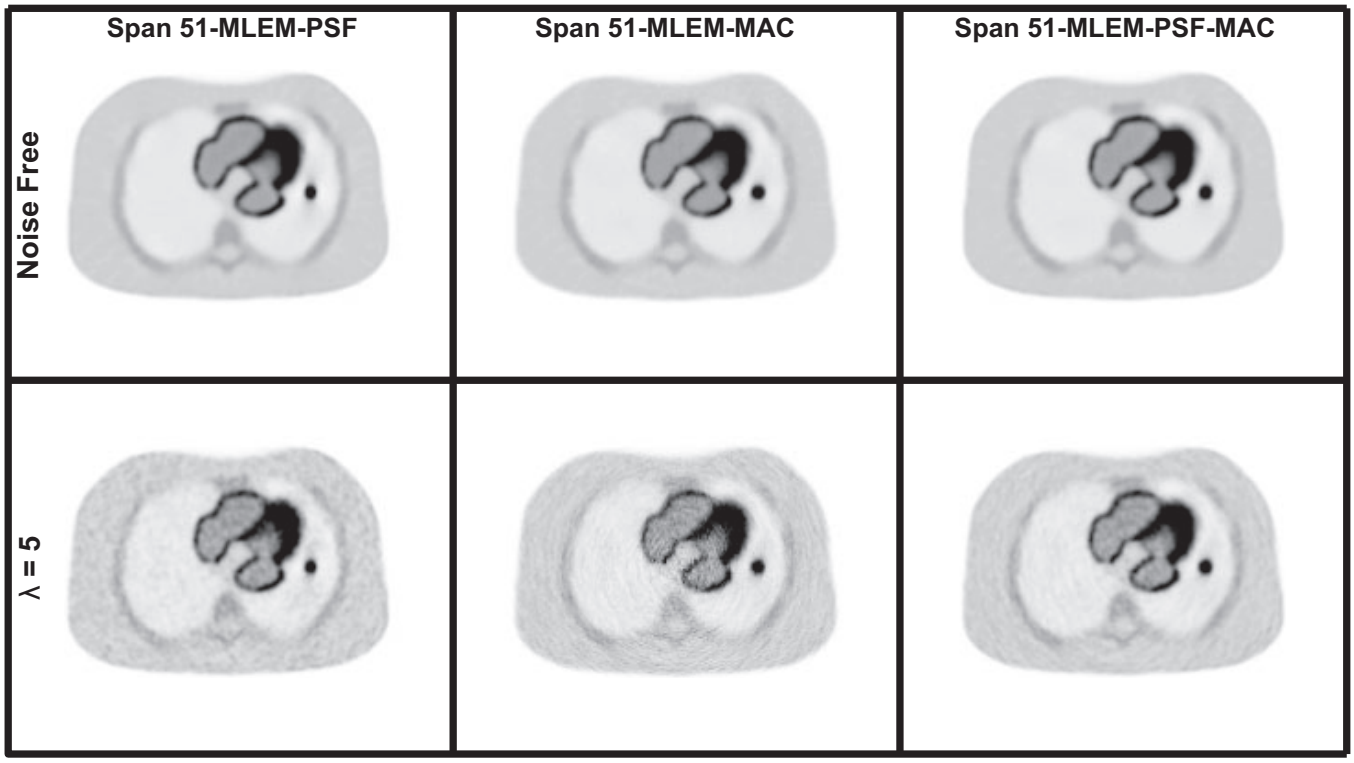

FIG. 16. Transverse slices of the span 51 reconstructed images from the NCAT phantom simulations which included the system PSF in the simulation. On the top row, the reconstructed images for noise-free simulations at iteration number 100 are shown; while on the bottom row, the reconstructions for the noisy simulations at iteration numbers 100, 70, and 100 are shown.

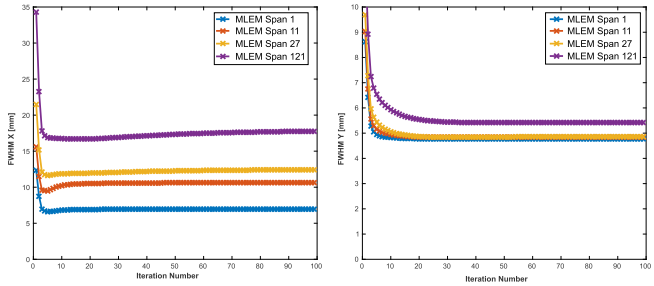

FIG. 17. FWHM in the x and y axes in slice number 30 for the line source acquisition for different levels of axial compression. [Color figure can be viewed at wileyonlinelibrary.com]

which axial compression modeling is a special case) changes the noise correlations in the reconstructed images. This is also observed in Fig. 16, where for the noise-free simulations the circular texture is not observed showing that this is an effect of the noise correlations arising from axial compression modeling. For the unmatched projector/backprojector (MLEM-MAC-U), the circular noise correlation was not present as it is only during the backprojection stage that the voxels are correlated in image-space.

The resolution recovery works well for axial compression of span values lower than 21 but for higher span values, the resolution cannot be compensated for completely and some artifacts are visible. A possible reason for this outcome is the large condition number of the system matrices when axial compression is applied. For high span numbers, the lower singular values drop steeply and this could be interpreted as an effective null space. As a result, the higher spatial frequencies cannot be recovered properly. This is observed in the SVD of the system matrix with axial compression modeling (MAC) in Fig. 4. This effective null space could be noise-dependent for certain span values, where the noise level is higher than the high-frequency components to recover. In the SVD plots, we could visualize the noise level as a horizontal line setting a threshold below which certain frequencies cannot be recovered. In Fig. 21, the COV and CR in the hot lesion of the reconstructed images of the NCAT phantom as a function of the iteration number are shown for a noise-free simulation and two noisy realizations with $\lambda = 5$ and $\lambda = 1$. For span 11 (top graph), the resolution loss is recovered completely for the three different realizations. For span 51 (bottom graph), the resolution loss cannot be totally compensated for, even for the noise free simulation. Therefore

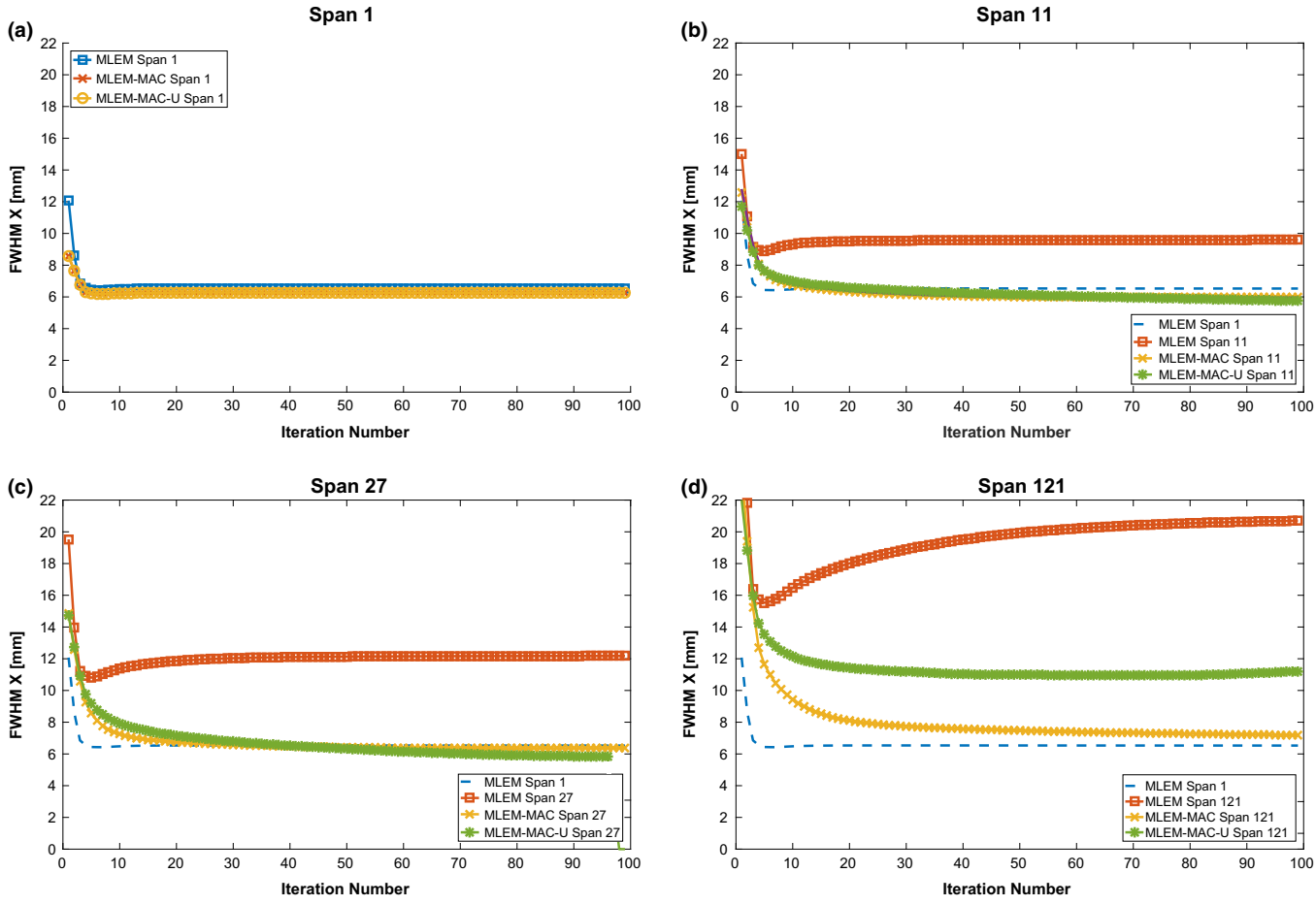

FIG. 18. FWHM in the x axis in the slice number 100 for span values of 1 (a), 11 (b), 27(c), and 121 (d) for the three reconstruction methods: MLEM, MLEM-MAC, and MLEM-MAC-U. [Color figure can be viewed at wileyonlinelibrary.com]

for span 51, this effective null space is not given by the noise, but by the axial compression itself (for a given sinogram and image size).

In Fig. 21, we also show the COV and CR for the MLEM and MLEM-MAC reconstructions of the noise-free span 5 simulation. In these results, it can be seen that the span 5 reconstructions do not outperform the span 1 reconstruction. Therefore, the apparent better performance of span 5 reconstruction in Figs. 9 and 10 was possibly a noise effect.

With respect to the reconstruction of the line source scan, the resolution was degraded only in the direction of x and z because the line source was located parallel to the xz plane. This is consistent with the PRF of systems that employ axial compression (MAC), where in the transverse planes the resolution is degraded mainly tangentially, as was shown previously (Fig. 6).

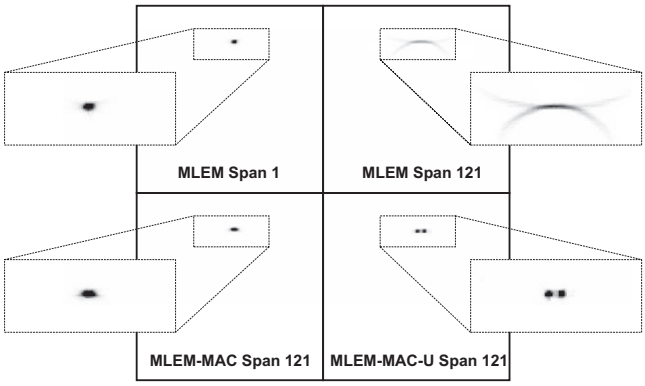

FIG. 19. Central slice of the reconstructed images of the line source scan at iteration number 60 for MLEM reconstruction for span 1 and 121 and for the MLEM-MAC and MLEM-MAC-U methods for the span 121 sinograms. A rectangular area centred on the source has been zoomed to aid visibility.

Regarding the computational cost, each reconstruction is proportional to the number of sinogram bins to process. For example, the span 1 reconstructions are approximately 5 times more computationally demanding than the span 11 reconstructions. However, in our specific implementation, where symmetries are not used, bins with zero counts in the emission sinogram do not need to be projected or backprojected and that reduces the difference to 3–4 times for a typical reconstruction with the sinogram sizes aforementioned. The implementation of the system matrix with axial compression involves using a span-1 projector and backprojector; for this reason, the computational cost is similar to a span-1 reconstruction (the additional axial compression operator is negligible in computational cost compared to the projection and backprojection). In the unmatched projector/backprojector reconstruction, where the axial compression is modeled only in the forward model, the computational cost is a span-1 projection and a span-a backprojection. For the case of our reconstruction library, the reconstruction times are considerably reduced as the backprojector is more than 5 times slower than the forward projector. Taking into account these considerations and the performance of the MLEM-MAC-U algorithm, the use of the unmatched projector/backprojector is a reasonable option to enhance contrast for axially-compressed scans when, for example, reconstruction times are critical such as in dynamic studies. However, special care needs to be taken for high span numbers, because in these cases the matrix $A_a^t A_{a-MAC}$ has a considerably larger condition number than the matched version (see Fig. 5), and therefore is prone to increase the noise and to introduce artifacts.

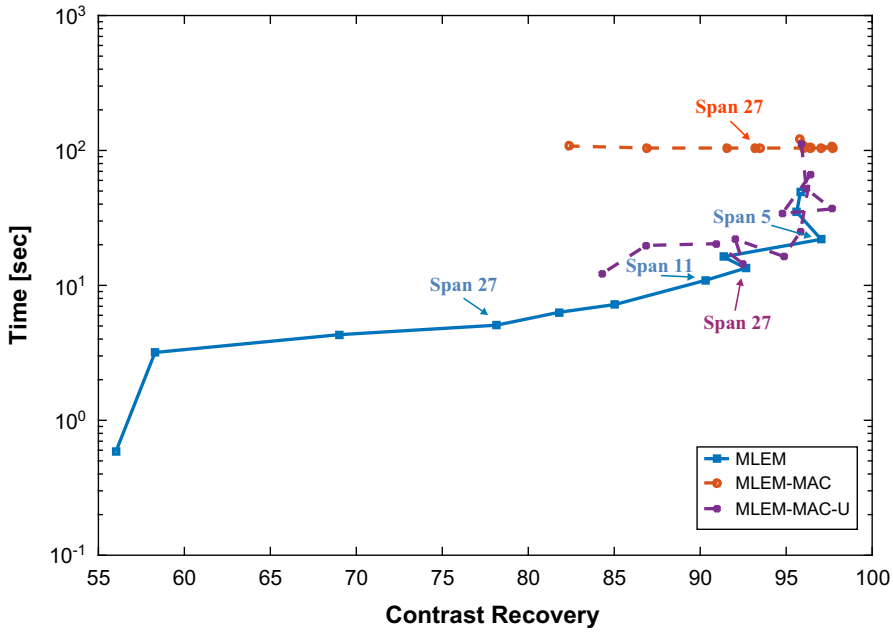

FIG. 20. Reconstruction time, in a logarithmic scale, vs contrast recovery in the reconstructed images of the NCAT phantom, for different choices of span, for the three reconstruction methods. [Color figure can be viewed at wileyonlinelibrary.com]

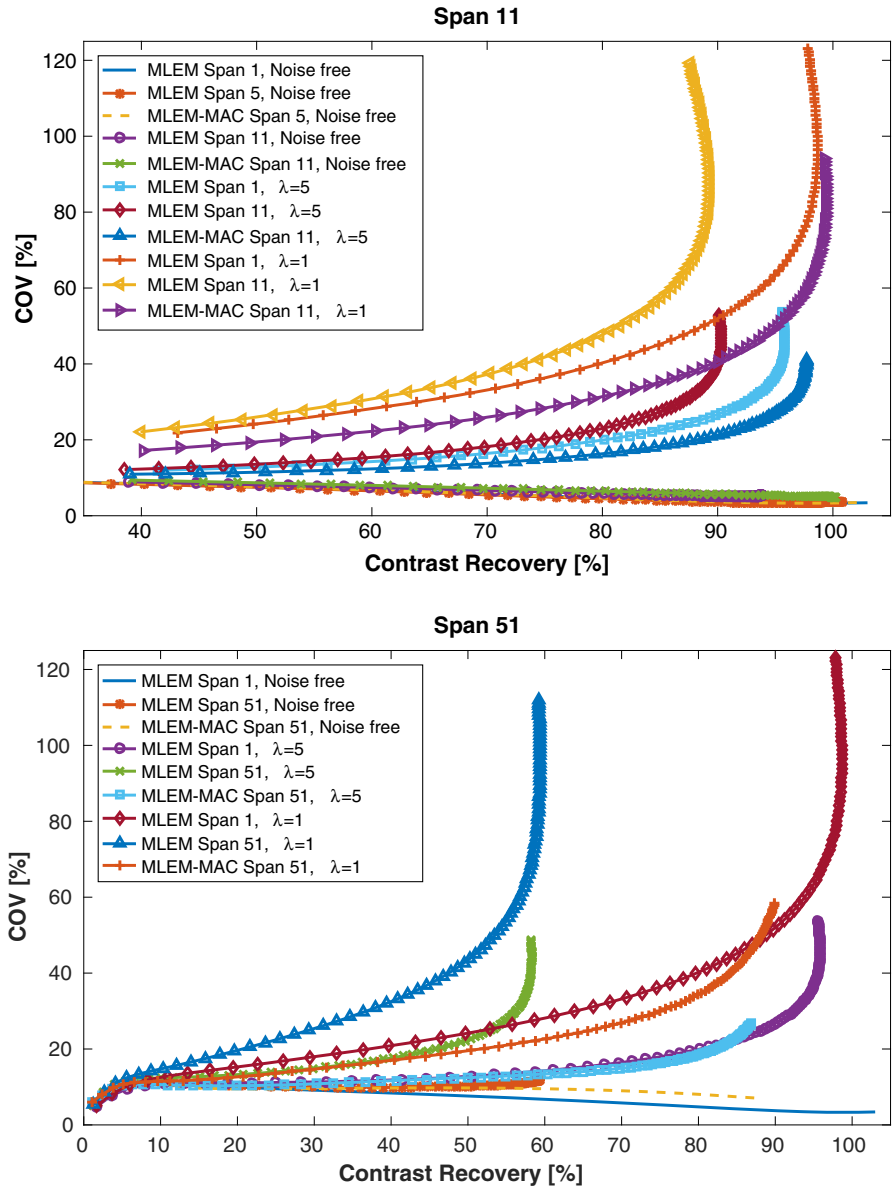

FIG. 21. COV and CR in the hot lesion of the reconstructed images of the NCAT phantom as a function of the iteration number for three different cases: noise-free, a noise realization with a sinogram bin mean value of 5, and a noise realization with a sinogram bin mean value of 1. Top: the results for span 11 sinograms and the methods MLEM and MLEM-MAC are compared with the span 1 reconstructions. Bottom: the same comparison is made for the span 51 sinograms. [Color figure can be viewed at wileyonlinelibrary.com]

5. CONCLUSION

Based on the simulation results, axial compression applied in PET has a negligible impact for span values of 3 and 5. For span 7, there was a loss of contrast of 5% points in only one of the phantoms but the computational cost is reduced considerably by a factor of 3. For span 11, which is the standard sinogram span for the Biograph mMR scanner, a loss of contrast of 5 to 10% points was observed in the two simulated phantoms. Therefore, an axial compression with span 7 seems to be a good compromise with respect to resolution and processing times, when this effect is not modeled in the system matrix, which is routinely the case in practice.

When the acquired data undergo axial compression, the degradation of the image resolution can be compensated for by modeling this effect in the system matrix at the expense of a considerably higher computational cost, but this can only be completely compensated for at lower span values (lower than 21 in our experiments). For higher span values, an improvement in the contrast was achieved, but it could not attain to that observed for the span 1 reconstructions. A hypothesis for not being able to accurately recover the resolution loss for high span values is the large condition number of the system matrix and the generation of an effective null space in the system. Furthermore, the methods that fully modeled the axial compression in the system

matrix showed a circular pattern that agrees with the inter-voxel correlations present in the system matrix. These inter-voxel correlations are larger for higher span values and artificially reduce the noise when a region-based metric is used.

The use of an unmatched projector/backprojector proved to be a practical solution to compensate for the spatial resolution degradation at a reasonable computational cost. However, for large span values, this can come at the cost of increased noise and also being more prone to artifacts when compared to the more correct method of using a matched projector/backprojector.

ACKNOWLEDGMENTS

This work was supported by the Engineering and Physical Sciences Research Council [grant number EP/M020142/1]. According to EPSRC's policy framework on research data, all simulation and real data results supporting this study will be openly available at https://www.zenodo.org/record/822827#.WWvQnSeQzCJ.

[a]Author to whom correspondence should be addressed. Electronic mail: martin.belzunce@kcl.ac.uk.

REFERENCES

1. Bendriem B, Townsend DW. *The Theory and Practice of 3D PET*. Dordrecht, Kluwer; 1998.
2. Surti S, Kuhn A, Werner ME, Perkins AE, Kolthammer J, Karp JS. Performance of philips gemini TF PET/CT scanner with special consideration for its time-of-flight imaging capabilities. *J Nucl Med*. 2007;48:471–480.
3. Jin X, Chan C, Mulnix T, et al. List-mode reconstruction for the biograph mCT with physics modeling and event-by-event motion correction. *Phys Med Biol*. 2013;58:5567–5591.
4. Kotasidis FA, Zaidi H. Experimental evaluation and basis function optimization of the spatially variant image-space PSF on the ingenuity PET/MR scanner. *Med Phys*. 2014;41:062501.
5. Nguyen NC, Vercher-Conejero JL, Sattar A, et al. Image quality and diagnostic performance of a digital PET prototype in patients with oncologic diseases: initial experience and comparison with analog PET. *J Nucl Med*. 2015;56:1378–1385.
6. Matthews J, Bailey D, Price P, Cunningham V. The direct calculation of parametric images from dynamic PET data using maximum-likelihood iterative reconstruction. *Phys Med Biol*. 1997;42:1155–1173.
7. Reader AJ, Sureau FC, Comtat C, Trébossen R, Buvat I. Joint estimation of dynamic PET images and temporal basis functions using fully 4D ML-EM. *Phys Med Biol*. 2006;51:5455–5474.
8. Daube-Witherspoon ME, Muehllehner G. Treatment of axial data PET in three-dimensional. *J Nucl Med*. 1987;28:1717–1724.
9. Lewitt RM, Muehllehner G, Karp JS. Threedimensional image reconstruction for PET by multi-slice rebinning and axial image filtering. *Phys Med Biol*. 1994;39:321–339.
10. Defrise M, Kinahan PE, Townsend DW, Michel C, Sibomana M, Newport DF. Exact and approximate rebinning algorithms for 3-D PET Data. *IEEE Trans Med Imaging*. 1997;16:145–158.
11. Vandenberghe S, Daube-Witherspoon ME, Lewitt RM, Karp JS. Fast reconstruction of 3D time-of-flight PET data by axial rebinning and transverse mashing. *Phys Med Biol*. 2006;51:1603–1621.
12. Defrise M, Panin V, Michel C, Casey ME. Continuous and discrete data rebinning in time-of-flight PET. *IEEE Trans Med Imaging*. 2008;27:1310–1322.
13. Panin VY, Kehren F, Michel C, Casey M. Fully 3-D PET reconstruction with system matrix derived from point source measurements. *IEEE Trans Med Imaging*. 2006;25:907–921.
14. Zeng GL, Gullberg GT. Unmatched projector/backprojector pairs in an iterative reconstruction algorithm. *IEEE Trans Med Imaging*. 2000;19:548–555.
15. Lee NY, Choi Y. Theoretical investigation on an unmatched backprojector for iterative reconstruction in emission computed tomography. *J Korean Phys Soc*. 2011;59:367.
16. Weng Y, Zeng GL, Gullberg GT. Iterative reconstruction with attenuation compensation from cone-beam projections acquired via non-planar orbit. *IEEE Trans Nuc Sci.* 1997;44:98–106.
17. Kadrmas DJ, Frey EC, Karimi SS, Tsui BM. Fast implementations of reconstruction-based scatter compensation in fully 3D SPECT image reconstruction. *Phys Med Biol*. 1998;43:857.
18. Feng B, King MA, Gifford HC, Pretorius PH, Zeng GL, Fessler JA. Modeling the distance-dependent blurring in transmission imaging in the ordered-subset transmission (OSTR) algorithm by using an unmatched projector/backprojector pair. IEEE NSS/MIC Conference Record, Puerto Rico; 2005:2690–2694.
19. Lazaro D, El Bitar Z, Breton V, Hill D, Buvat I. Fully 3D Monte Carlo reconstruction in SPECT: a feasibility study. *Phys Med Biol*. 2005;50:3739.
20. Rahmim A, Qi J, Sossi V. Resolution modeling in PET imaging: theory, practice, benefits, pitfalls. *Med Phys*. 2013;40:064301.
21. Alessio AM, Rahmim A, Orton CG. Resolution modelling enhances PET imaging. *Med Phys*. 2013;40:120601.
22. Nuyts J. Unconstrained image reconstruction with resolution modelling does not have a unique solution. *EJNMMI Phys*. 2014;1:98.
23. Tong S, Alessio AM, Thielemans K, Stearns C, Ross S, Kinahan PE. Properties and mitigation of edge artifacts in PSF-based PET reconstruction. *IEEE Trans Nuc Sci*. 2011;58:2264–2275.
24. Delso G, Fürst S, Jakoby B, et al. Performance measurements of the Siemens mMR integrated whole-body PET/MR scanner. *J Nuc Med*. 2011;52:1914–1922.
25. Shepp LA, Vardi Y. Maximum likelihood reconstruction for emission tomography. *IEEE Trans Med Imaging*. 1982;1:113–122.
26. Belzunce MA, Reader AJ. Time-invariant component-based normalization for a scanner simultaneous PET-MR. *Phys Med Biol*. 2016;61:3554–3571.
27. Comtat C, Bataille F, Michel C, et al. OSEM-3D reconstruction strategies for the ECAT HRRT. In: *IEEE NSS/MIC Conference Record, 2004*. Rome: IEEE; 2004:3492–3496.
28. Belzunce MA, Verrastro CA, Venialgo E, Cohen IM. Cuda parallel implementation of image reconstruction algorithm for positron emission tomography. *Open Med Img J*. 2012;6:108–118.
29. Leahy R, Qi J. Statistical approaches in quantitative positron emission tomography. *Stat Comput*. 2000;10:147–165.
30. Segars WP, Lalush DS, Tsui BMW. A realistic splinebased dynamic heart phantom. *IEEE Trans Nuc Sci*. 1999;46:503–506.
31. Kudo H, Noo F, Defrise M. Cone-beam filtered-backprojection algorithm for truncated helical data. *Phys Med Biol*. 1998;43:2885.
32. Reader AJ, Julyan PJ, et al. EM algorithm system modeling by image-space techniques for PET reconstruction. *IEEE Trans Nucl Sci*. 2003;50:1392–1397.